BOLETIN DE LA SOCIEDAD ESPAÑOLA DE
Cerámica y Vidrio
www.elsevier.es/bsecv

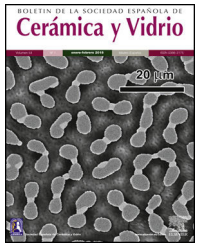

Obtaining characterization and *in vitro* behavior of 3D multilayer ceramic scaffolds $Ca_2SiO_4/Ca_2P_6O_{17}/Ca_2SiO_4$-XSr

Karina Salazar[a], *Ángel Murciano*[b,*], *Pablo Velásquez*[a], *Piedad N. De Aza*[a]

[a] *Instituto de Bioingeniería, Universidad Miguel Hernández, Avda. Ferrocarril S/n, Elche, Alicante 03202, Spain*
[b] *Departamento de Materiales, Óptica y Tecnología Electrónica, Universidad Miguel Hernández, Avda. Universidad S/n, Elche, Alicante 03202, Spain*

ARTICLE INFO

Article history:
Received 22 August 2024
Accepted 5 December 2024
Available online 28 January 2025

Keywords:
Glass-ceramic
Multilayer scaffolds
Sol–gel
Bioactivity

ABSTRACT

In this study, 3D multilayer scaffolds were fabricated by sol–gel and polymeric replication methods. The principal objective was to fabricate scaffolds based on a core of $Ca_2SiO4/Ca_2P_6O_{17}$ (C_2S/P_6) to obtain mechanical resistance following by external layers with composition Ca_2SiO_4 (C_2S) doped with several amount of $SrCO_3$ (Sr = 0–2.5 wt%) to generate modulated bioactivity.

This scaffold was characterized from the physical, chemical and mineralogical point of view. Finally, the effect of the dopant on the surface morphology and how it affects the bioactivity was carried out according to the ISO 23317.2017 standard.

The obtained scaffolds exhibited an open porosity of 80–90% and a maximum mechanical strength of 1.2 ± 0.1 MPa. The scaffolds containing Sr^{2+} demonstrated bioactivity that could be modulated according to the Sr content. The results revealed that bioactivity occurred only when the scaffolds were coated with outer layers of strontium. Scaffolds doped with 1 and 1.5 wt% Sr displayed bioactivity after 3 days in simulated body fluid (SBF), while the 2.5 wt% Sr sample did not show bioactivity at any time.

Obtención, caracterización y comportamiento *in vitro* de andamios 3D cerámicos multicapa de composición $Ca_2SiO_4/Ca_2P_6O_{17}/Ca_2SiO_4$-XSr

Palabras clave:
Vitrocerámica
Andamios multicapa
Sol–gel
Bioactividad

RESUMEN

En este estudio, se fabricaron andamios multicapa 3D mediante el método de sol-gel y replicación polimérica. El objetivo principal fue fabricar andamios basados en un núcleo de $Ca_2SiO_4/Ca_2P_6O_{17}$ (C_2S/P_6) para obtener resistencia mecánica seguida de capas externas con composición Ca_2SiO_4 (C_2S) dopadas con varias cantidades de $SrCO_3$ (Sr = 0–2,5% en peso) para generar bioactividad modulada.

* *Corresponding author.*
E-mail address: angel@dite.umh.es (Á. Murciano).
https://doi.org/10.1016/j.bsecv.2024.12.001

Este andamio se caracterizó desde el punto de vista físico, químico y mineralógico. Finalmente, se llevó a cabo el estudio del efecto del dopante sobre la morfología superficial y cómo afecta a la bioactividad de acuerdo con la norma ISO 23317.2017.

Los andamios obtenidos presentaron una porosidad abierta del 80-90% y una resistencia mecánica máxima de 1,2 ± 0,1 MPa. Los andamios dopados con Sr^{2+} mostraron una bioactividad que puede modularse en función del contenido de Sr. Los resultados revelaron que la bioactividad sólo se producía cuando los andamios estaban recubiertos con capas externas de Sr. Los andamios dopados con 1 y 1,5% en peso de Sr mostraron bioactividad después de 3 días en suero fisiológico artificial, mientras que la muestra con 2,5% en peso de Sr no fue bioactiva en ningún momento.

Introduction

The bone system fulfills very important functions in the human body, since it protects the internal organs, it is a structural support, besides allowing the movement of the body. However, over time this system has been affected by bone diseases such as cancer, infections, osteoporosis and also fractures, where a problem is generated reducing the quality of life [1]. In recent years, research for alternative bone grafts to autologous and allogeneic bone grafts has increased, with emphasis on grafts derived from ceramic materials, such as pyrophosphates, phosphates, and sulfates, due to their mechanical properties, antimicrobial and biodegradable qualities, as well as their osteoinductive and osteoconductive properties. These grafts also promote osseointegration and can bind to bone through the formation of hydroxyapatite (HA) on the surface. Additionally, they can also act as support for essential enzyme cofactors during bone tissue development [2–4].

Currently, C_2S dicalcium silicate based materials are recognized for bone regeneration due to their ability to degrade and release Ca^{2+} and Si^{4+} ions, which are known for their biocompatibility, osteogenesis and therefore Si may play a direct role in the bone mineralization process [5]. In addition, another recent research has indicated that silicon (Si) has the ability to stimulate the proliferation and differentiation of bone marrow mesenchymal stromal cells, as well as enhance collagen synthesis [6]. But it is worth mentioning that these ceramics lack mechanical properties and are difficult to manipulate.

For this reason, some research has focused on the development of glass ceramics (GC) that increases the strength of these materials. This is due to the advantages they possess over base glasses or traditional ceramics in terms of physical, chemical, biological and mechanical properties [7]. These materials are developed through the controlled crystallization of glass. This crystallization process is achieved by a precise heat treatment applied to specific glasses, such as phosphates (P_2O_5), which induces the gradual formation of crystalline structures within the material. This procedure involves heating the glass above its glass transition temperature, thus allowing molecular rearrangement to initiate nucleation. Through controlled cooling, crystal growth is facilitated, determining their size, distribution and composition [8–10]. In addition, these vitrified materials have versatile properties that can be modified to suit specific applications through doping. Currently, different ions such as zinc (Zn) [11], silver (Ag) [12], magnesium (Mg) [12], strontium (Sr) [13] and lithium (Li) [14] have been employed for bone tissue regeneration [15].

Pertinent research has identified strontium (Sr) as a dependable element capable of aiding bone tissue regeneration by boosting osteoblast activity and diminishing osteoclast function. Due to the analogous chemical properties of Sr and Ca and their ionic radii (Sr = 1.16 Å and Ca = 0.94 Å), replacing Ca with Sr has consistently been suggested to leverage the synergistic effects of Sr and Ca in Ca–Si based glass ceramics [14,16].

Additionally, strontium (Sr) is recognized for its therapeutic application in stimulating bone regeneration. Consequently, it can be inferred that incorporating Sr would result in multifunctional benefits, such as reducing bone resorption and accelerating bone remodeling by promoting the replication of preosteoblastic cells and lowering osteoclast activity [17,18].

Bone density behaves differently at different stages of life. For example, bone density increases in the early stages of life, reaching the highest density in early adulthood. Thereafter, bone density is maintained throughout most of adulthood until old age, when bone density begins to decline due to degenerative biological processes. For this reason, the requirements of a scaffold are different depending on the age of the patient. In this regards it is necessary to modulate the bioactivity to adapt the implant to the patient's needs, thus creating personalized medicine.

In this paper, scaffolds consist of a core made of glass-ceramic (C_2S/P_6), surrounded by external layers of C_2S ceramic doped with varying amounts of $SrCO_3$ (Sr = 0–2.5 wt%). The aim is to modify the scaffold surface to modulate *in vitro* bioactivity, in accordance with the ISO 23317:2017 standard [19], with the goal of evaluating their potential for future bone implants applications.

Materials and methods

The new 3D scaffolds were made by sol–gel and polymeric sponge replication methods. A polyurethane mold sponges with a porosity of 20 ppi and dimensions 12 mm Ø × 0.9 mm

Table 1 – Compositions (wt%) of the 3D scaffold.

Sample	Core		External layers			Doped layer		
	TEOS	$CaCO_3$	TEP	$CaCO_3$	Li_2CO3	TEOS	$CaCO_3$	$SrCO_3$
3D[C_2S]	52.72	47.23	–	–	–	–	–	–
3D[C_2S/P_6-P_6]	52.72	47.23	82	16	2	–	–	–
3D[C_2S/P_6-P_6]C_2S	52.72	47.23	82	16	2	52.72	47.23	–
3D[C_2S/P_6-P_6]C_2S-0.5Sr	52.72	47.23	82	16	2	52.54	47.11	0.35
3D[C_2S/P_6-P_6]C_2S-1Sr	52.72	47.23	82	16	2	52.35	46.95	0.7
3D[C_2S/P_6-P_6]C_2S-1.5Sr	52.72	47.23	82	16	2	52.17	46.79	1.03
3D[C_2S/P_6-P_6]C_2S-2.5Sr	52.72	47.23	82	16	2	51.82	46.47	1.71

All the preparations were carried out with 20 mL of distilled water, 5 mL of ethanol and 1 mL of HCl.

long (Eurofoam-Germany-PU), were coated with a sol–gel solution formed by: 98% Tetraethyl Orthosilicate, Aldrich (TEOS) as a silicon source; ≥99% calcium carbonate ($CaCO_3$, Sigma) as a calcium source; ≥99.8% triethy phosphate (TEP, Aldrich) as a phosphorus source; ≥99% lithium carbonate ($LiCO_3$, Sigma) and 99% carbonate de strontium ($SrCO_3$ Sigma–Aldrich). Table 1 summarizes the chemistry composition each layer of the 3D multi-layer scaffolds.

In order to obtain the most internal layer (3D[C_2S]) appropriate reactants above mentioned mixed under continuous stirring at room temperature for 15 min to allowed to achieve a transparent solution with 5 mL of 97% ethanol (Carlo Erba), 20 mL of distilled water and 1 mL of 37% hydrochloric acid (HCl-Carlo Erba) until obtained a pH 3. The polyurethane sponges were submerged between 30 and 50 times and dried in the oven for 10 min at 150 °C every time. Finally, to synthesize the 3D[C_2S] ceramic was heat treatment in an oven at 1050 °C at a heating rate of 19 °C/h for 55 h maintaining this temperature for 8 h. Following of the free descent in the oven to room temperature.

A second layer of a glassy phase $Ca_2P_6O_{17}$ (P_6) were prepared with TEP, ethanol, lithium carbonate, hydrochloric acid and distilled water. The 3D[C_2S] ceramic was coated 10 times with this solution, dried at 150 °C for 10 min and the new 3D[C_2S/P_6] scaffolds were sintered for 1050 °C/55 h maintaining this temperature for 8 h. Following of the free descent in the oven to room temperature. This process se realize two times to obtain a multilayer core of 3D[C_2S/P_6-P_6] perfectly manageable. To remove the excess of glass phase, the core 3D[C_2S/P_6-P_6] was chemical etching by immersing it in 50 mL of SBF during 2 h a 37 °C [19].

After obtaining a highly manageable core scaffold 3D[C_2S/P_6-P_6] a sol–gel solution of an external layer of C_2S with and without Sr^{2+} (Sr = 0–2.5 wt%) was made. A first solution was prepared by mixing 12.95 mL of TEOS, 5 mL of ethanol (97%), 20 mL of distilled water, 1 mL of 37%HCl until obtain pH 3. The solution was stirred for 20 min to allow the hydrolysis of precursors. A second solution was prepared with 11.62 g of calcium carbonate, 10 mL of distilled water, and 50 mL of hydrochloric acid. The final solution reaches a pH 3. Both solutions were mixed under continues stirring for 15 min to achieve transparent solution in which the core was immersed 5 times. Finality, the scaffolds 3D[C_2S/P_6-P_6]C_2S was dried a 150 °C for 10 min and sintered under the same conditions as above.

In the scaffold doped with strontium 3D[C_2S/P_6-P_6]C_2S-XSr (Sr = 0–2.5 wt%) a strontium carbonate was used instead calcium carbonate. The amounts of strontium added in each solution were 0.35 g (0.5 wt%), 0.7 g (1 wt%), 1.03 g (1.5 wt%) and 1.77 g (2.5 wt%). Afterward, 3D[C_2S/P_6-P_6]C_2S-XSr scaffolds were sintered at 1050 °C at a heating rate of 19 °C/h for 55 h maintaining this temperature for 8 h. Following of the free descent in the oven to room temperature

Scaffolds characterization

The evaluation of the cores 3D[C_2S] and 3D[C_2S/P_6-P_6], and the 3D[C_2S/P_6-P_6]C_2S-XSr multilayer scaffolds' morphological composition was performed using X-ray diffraction (XRD, Bruker-AXR D8 Advance) with Cu-Kα radiation (1.5418740 Å). The data collection range was 10–50° (2θ) with 0.02° steps, and each step was counted for 8 s. The X-ray tube operated at 40 kV and 30 mA. The diffractograms were then compared with the Crystallography Open Database (COD).

Subsequently, Fourier Transform Infrared Spectroscopy (FTIR) analysis was conducted with a Thermo Scientific Nicolet iS5 spectrometer, fitted with an iD5 ATR accessory. The spectra were collected between 550 cm^{-1} and 1450 cm^{-1} at room temperature, with a resolution of 4 cm^{-1} and using 64 scans.

The macroscopic features of the scaffolds were initially examined with a Nikon digital camera. This was followed by a detailed morphological study using Scanning Electron Microscopy with Energy Dispersive X-Ray Spectroscopy (SEM-EDX) on a Hitachi S-3500N, using the INCA system from Oxford Instruments Analytical. Palladium coating was applied to all samples prior to analysis.

The porosity and pore distribution of the 3D scaffolds were evaluated by the Mercury Porosimetry Technique (Quantachrome Poremaster, for WINDOWS® DATA REPORT VERSION 8.1) for pores between 300 and 0.001 μm and pressure range between 66.6 bar and 4104.84 bar. The total porosity was evaluated by Archimedes Principle in mercury.

The mechanical strength of the scaffolds was evaluated of compressive strength using Microtest SCM3000 mechanical testing equipment. The tests were performed by applying loads to 20 cylindrical scaffolds (8.5 mm diameter, 10.2 mm height) at a rate of 1.00 mm/min until the scaffold was completely broken.

The scaffolds with the size above indicate were used for the bioactivity test. They were immersed in a SBF solution

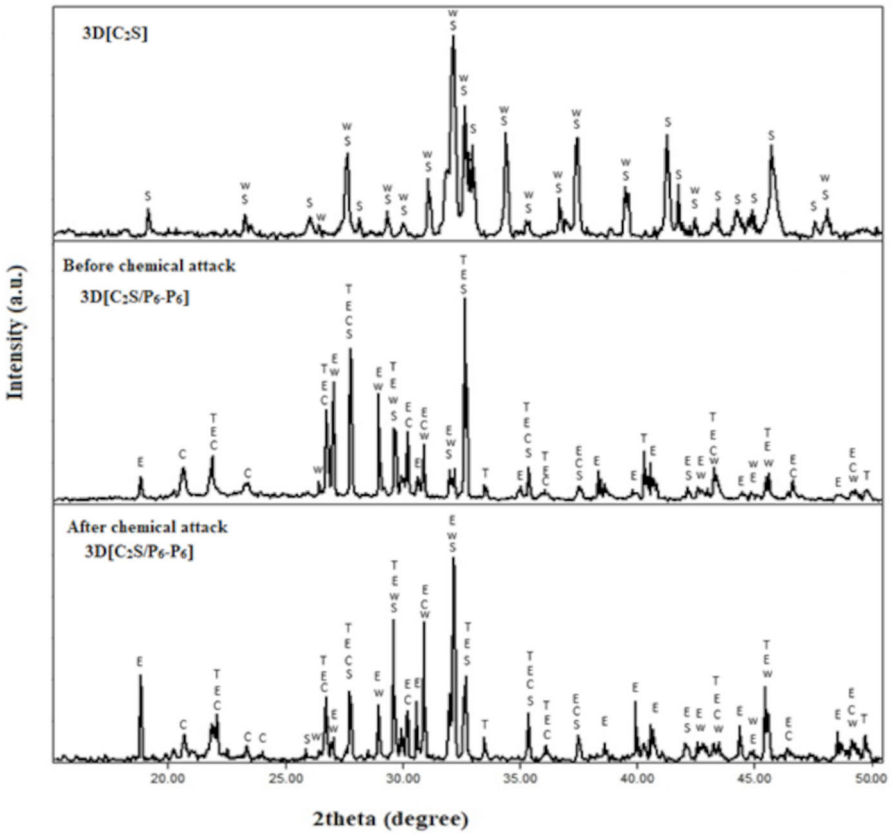

Fig. 1 – The XRD diffraction patterns of the cores 3D[C_2S] and 3D[C_2S/P_6-P_6] before and after chemical attack. [S: Ca_2SiO_4, W: $CaSiO_3$, E: $Ca_2P_2O_7$, C: SiO_2 and T: $Ca_3P_2O_8$].

prepared according to ISO 23317:2027 [19]. The scaffolds were submerged in 50 mL of SBF (pH 7.4) at 37 °C in a water bath for 1, 3, 7, 14, and 21 days. After each period, the scaffolds were dried at 60 °C for 24 h and their bioactivity was assessed by SEM-EDX. Changes in the concentrations of calcium (Ca), silicon (Si), and phosphorus (P) ions were analyzed using inductively coupled plasma optical emission spectrometry (PerkinElmer Optima 2000^{TM} ICP-OES).

Results

Fig. 1 shows the XRD patterns of the cores 3D[C_2S] and 3D[C_2S/P_6-P_6] before and after chemical attack with SBF. The core 3D[C_2S] presents two phases that correspond to calcium silicate (Ca_2SiO_4) (COD-96-154-6028) and wollastonite ($CaSiO_3$) (COD-96-900-8152).

The XRD of the outer layers of the core 3D[C_2S/P_6-P_6], show the same phases of the inner core plus calcium diphosphate ($Ca_2P_2O_7$) (COD 96-100-1557), cristobalite (SiO_2) (COD 96-900-8228) and tricalcium phosphate ($Ca_3P_2O_8$) (COD 96-151-7239). There is not deference in relation with the phases presents before and after chemical attack. Only a slight change in intensity was observed after chemical etching.

Fig. 2 shows the XRD patterns of the multilayer scaffolds 3D[C_2S/P_6-P_6]C_2S and 3D[C_2S/P_6-P_6]C_2S-1Sr, as representative of all doped scaffolds.

The 3D[C_2S/P_6-P_6]C_2S scaffold shows the characteristic peaks of the phases found in the core being calcium diphosphate ($Ca_2P_2O_7$) (COD 96-100-1557) the main phase.

In addition, 3D[C_2S/P_6-P_6]C_2S-1Sr exhibited characteristic peaks of the phases found in the core, as well as a new phase containing Sr. This phase corresponds to the non-stoichiometric calcium/strontium silicate ($Ca_{62.13}O_{168}P_{42}Sr_{6.27}$) (COD 96-434-1177). Additionally, there was a decrease in peaks corresponding to the calcium diphosphate phase and a significant increase in tricalcium phosphate. The diffractograms of the scaffolds doped with 1.5 wt% and 2.5 wt% strontium show the same phases as the scaffold 3D[C_2S/P_6-P_6]C_2S-1Sr (data not shown).

The spectra of the materials revealed several signals in the 1000–1300 cm^{-1} range (Fig. 3). These signals are due to the combined asymmetric stretching of Si—O—Si and PO_4^{3-} groups, which generally show vibrational modes in the 1000–1300 cm^{-1} range and 1000–1100 cm^{-1} range [20–22] respectively. The presence of the Si—O—Si group was also confirmed by a signal at 800 cm^{-1}, corresponding to a symmetric stretching or bending vibration [23]. It is noteworthy that only the core 3D[C_2S/P_6-P_6] exhibits a band at 1260 cm^{-1}, which correlates with the polymerization of the Si—OH groups, resulting in the formation of Si—O—Si bonds [22].

Signals were also observed at 956 cm^{-1} and 971 cm^{-1}, along with those at 524 cm^{-1} and 611 cm^{-1}, which are associated with the symmetric stretching and bending vibrations of the

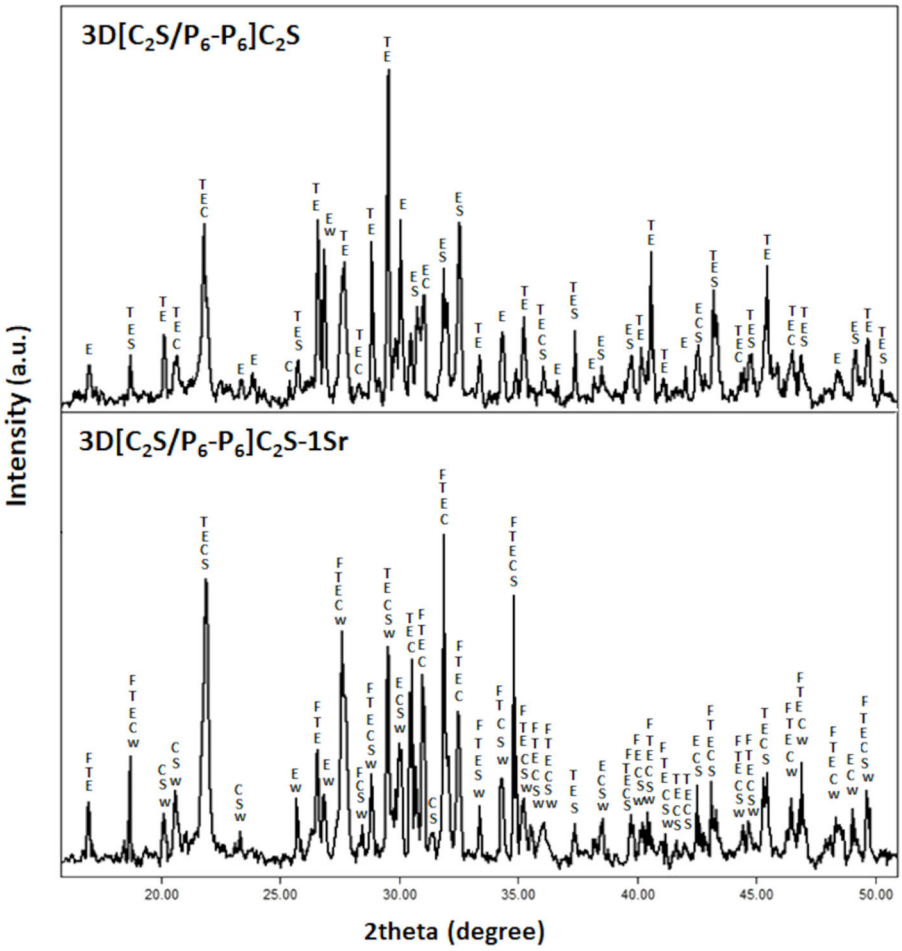

Fig. 2 – The XRD diffraction patterns of the multilayer scaffolds, 3D[C_2S/P_6-P_6]C_2S and 3D[C_2S/P_6-P_6]C_2S-1Sr. [S: Ca_2SiO_4, W: $CaSiO_3$, E: $Ca_2P_2O_7$, C: SiO_2 and T: $Ca_3P_2O_8$ and F: $Ca_{62.13}O_{168}P_{42}Sr_{6.27}$].

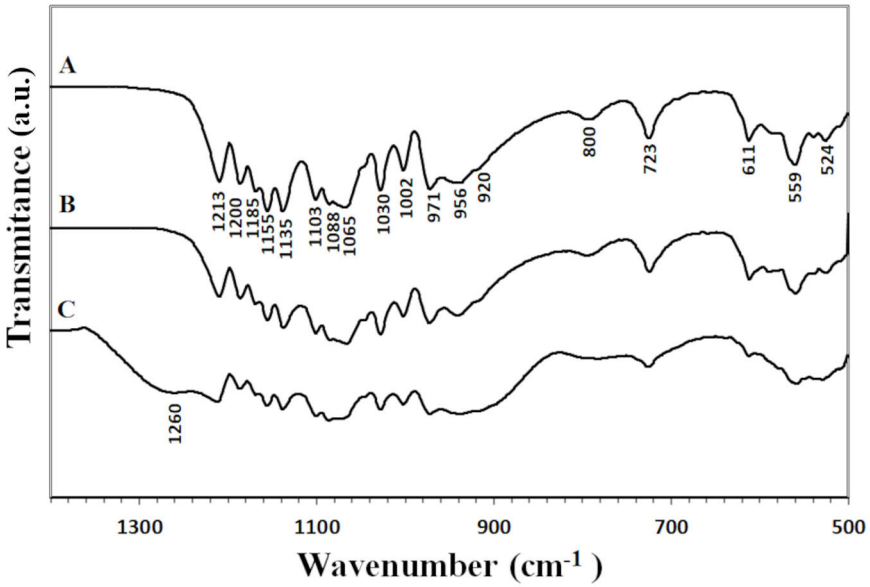

Fig. 3 – The scaffold's FTIR spectra. (A) Core 3D[C_2S/P_6-P_6], (B) 3D[C_2S/P_6-P_6]C_2S and (C) 3D[C_2S/P_6-P_6]C_2S-1Sr.

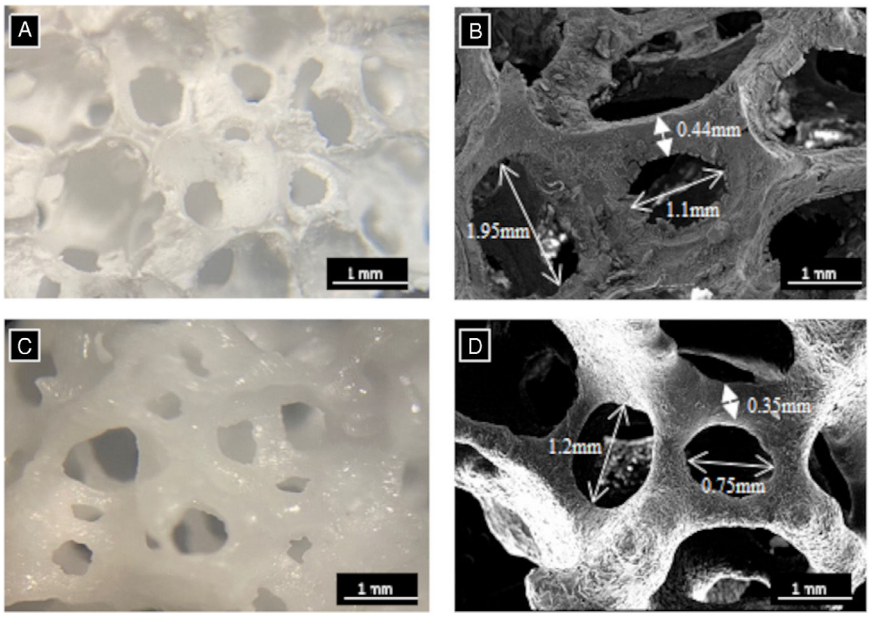

Fig. 4 – Optical images and of SEM micrographs of core scaffolds: (A) and (B) 3D[C_2S] and (C) and (D) 3D[C_2S/P_6-P_6].

PO_4^{3-} group. These vibrations are reported in the ranges of 900–970 cm^{-1} and 520–660 cm^{-1}, respectively [21]. Additionally, the pyrophosphate group ($P_2O_7^{4-}$) was identified by signals at 1213 cm^{-1}, 920 cm^{-1}, and 723 cm^{-1} [24].

Scaffolds that were coated with and without Sr ions showed a decrease in signal intensity over the entire spectrum range (500–1200 cm^{-1}). Special attencion to the signals around 1002 cm^{-1} persisted, which could be attributed to the presence of Si—O—Si and PO_4^{3-} groups. Also increase in the intensity of the peaks at 800 cm^{-1}, possibly associated with the vibration of the Si—O—Si and PO_4^{3-} group or the Si—O—2NBO at 900 group, which implies a SiO_4 bond with two non-bonding oxygens (Fig. 3).

Fig. 4A and C presents the macroscopic morphology of the core scaffolds 3D[C_2S] and 3D[C_2S/P_6-P_6] respectively showing an open porosity of cylindrical shape which is consistent with the polymeric model used to obtain the scaffolds.

This morphology was confirmed microscopically in Fig. 4B and D, with the presence of a random distribution of pores and struts. The macropores measured between 2 and 0.75 mm in size while the struts had a thickness ranging from 0.35 to 0.45 mm. The measurements of the macropores and the struts were taken from 10 measures per core scaffold in quadruplicate in each sample. Additionally, the scaffolds exhibited complete densification following heat treatment, thus ensuring adequate manipulability.

The difference between the innermost layer of the core formed by a C_2S ceramic and the outermost layer formed by the P_6 glass can be perfectly observed in Fig. 5. Fig. 5A shows a surface of the innermost layer without a clear or well-defined microstructure. The core 3D[C_2S/P_6-P_6] (Fig. 5B) shows a microstructure in the form of polyhedral grains of $Ca_2P_2O_7$ (Δ) coated with a glass (•). Finally, Fig. 5C shows the glass partially removed after chemical etching, and the polyhedral grains are observed protruding from the surface due to the lack of glass. According to EDX, the grains shown to be of calcium pyrophosphate (*) and the strontium is not detected because it is below the detection limit of the equipment. On the sample surface, another observed structure was bright precipitates (♣), which were identified through EDX analysis as being composed entirely of silicon.

Fig. 6 shows the SEM photographs the scaffolds 3D[C_2S/P_6-P_6]C_2S and 3D[C_2S/P_6-P_6]C_2S-1Sr as representative of the all doped scaffolds.

The microstructure of the 3D[C_2S/P_6-P_6]C_2S scaffolds (Fig. 6A) shows an external layer of polyhedral grains (*) homogeneously distributed over the entire surface of the scaffolds (without the presence of glass phase between the grains) the results showed a Ca/P ratio of about 1 corresponding mainly to calcium pyrophosphate.

In Fig. 6B, the microstructure of the 3D[C_2S/P_6-P_6]C_2S-1Sr is depicted, showing a consistent arrangement of hexagonal grains. This pattern is associated with the presence of tricalcium phosphate (♠), characterized by a Ca/P ratio of around 1.5.

The results were validated by comparing them with the results derived from the XRD patterns of the samples, as illustrated in Fig. 2.

Fig. 7 shows the results obtained using the Mercury Porosimetry Technique to analyze the level and distribution of porosity, and Table 3 shows the percentages of pore types, as well as other physical properties of the core 3D[C_2S/P_6-P_6] and also the scaffolds 3D[C_2S/P_6-P_6]C_2S and 3D[C_2S/P_6-P_6]C_2S-1Sr, as representative of the other doped scaffolds. The main differences are between the core 3D[C_2S/P_6-P_6] and the scaffolds 3D[C_2S/P_6-P_6]C_2S, while the dopant does not have a significant influence (Table 2).

In Fig. 7A the 3D[C_2S/P_6-P_6] core had mostly intraparticle pores, with two main ranges of intruded mercury. The first with a pore distribution from 212 μm and 32.91 μm and the second region with pores between 4.371 μm and 0.01 μm. In contrast, the 3D[C_2S/P_6-P_6]C_2S scaffold shows

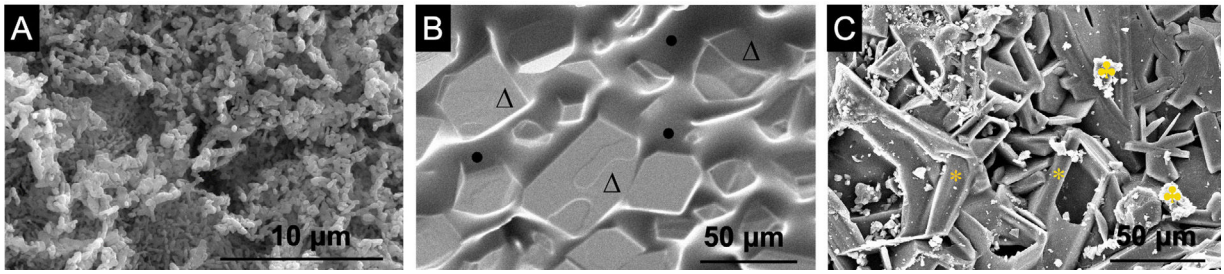

Fig. 5 – SEM micrographs of the: (A) core 3D[C_2S], (B) core 3D[C_2S/P_6-P_6] before chemical attack, (C) core 3D[C_2S/P_6-P_6] after chemical attack [EDX: (Δ) $Ca_2P_2O_7$, (●) glass, (*) calcium pyrophosphate (♣) silicon].

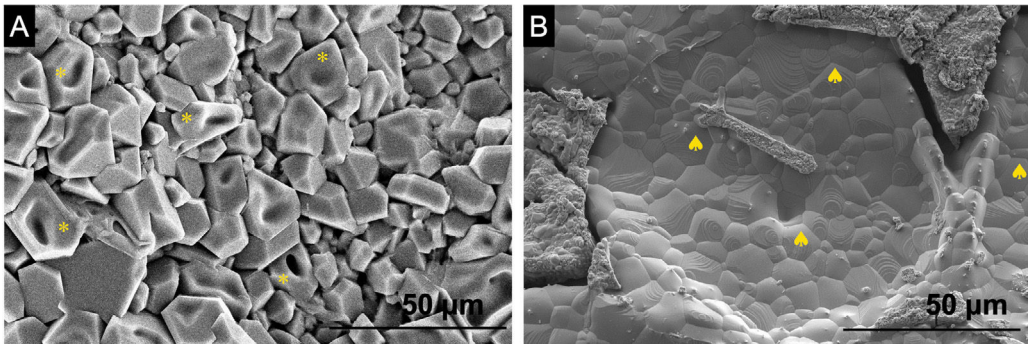

Fig. 6 – SEM micrographs of the: (A) scaffold 3D[C_2S/P_6-P_6]C_2S and (B) scaffold 3D[C_2S/P_6-P_6]C_2S-1Sr. [EDX: (*) calcium pyrophosphate, (♠) tricalcium phosphate].

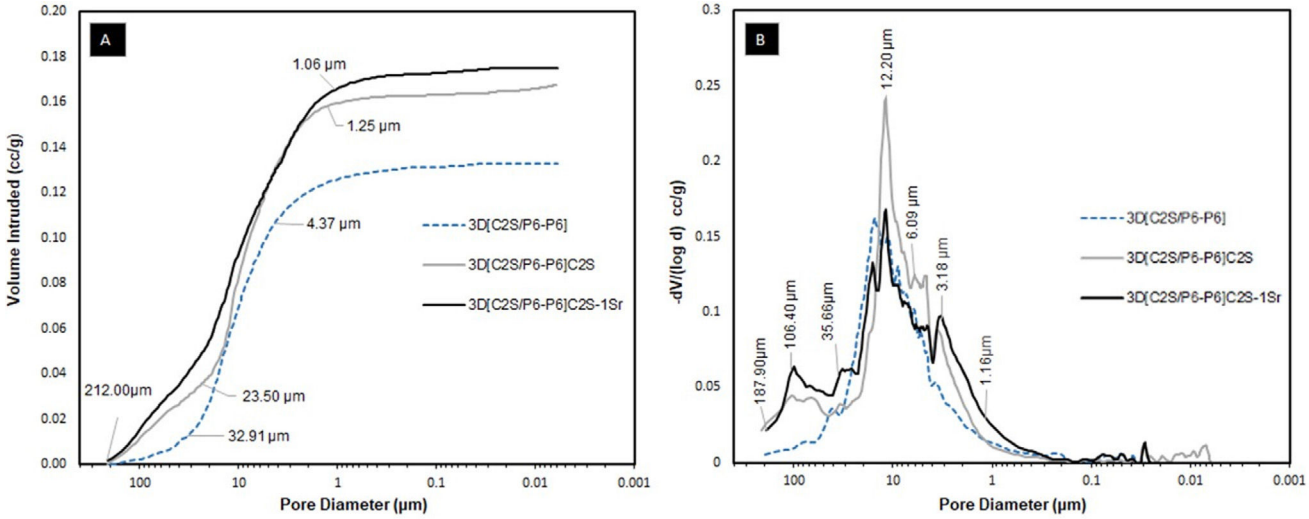

Fig. 7 – Mercury porosimetry curves: (A) Cumulative and (B) Differential intrusion *vs.* pore diameter in different scaffolds.

ranges approximately between 212 µm and 1.25 µm and the 3D[C_2S/P_6-P_6]C_2S-1Sr scaffold presented ranges between 212 µm and 1.06 µm.

Fig. 7B shows that the 3D[C_2S/P_6-P_6], core presents a homogeneous pore distribution between 50 and 3 µm. While the 3D[C_2S/P_6-P_6]C_2S and 3D[C_2S/P_6-P_6]C_2S-1Sr scaffolds present a bimodal distribution with a first group of pores larger than 35.66 µm and a second group with higher number of pores above in the range 15–1 µm having a mean peak around 12.20 µm. This technique gives information of pores less than 300 µm, thus 3D[C_2S/P_6-P_6]C_2S and 3D[C_2S/P_6-P_6]C_2S-1Sr scaffolds present similar porosity 31.66% and 32.15% (Table 3). Additionally, the Archimedes Principle gives a total porosity of 87 and 86% greater than 300 µm.

In relation to the compressive strength of the core and scaffolds, Table 3 show that the core 3D[C_2S/P_6-P_6] present values of 1.2 ± 0.1 MPa, scaffold 3D[C_2S/P_6-P_6]C_2S was 1.0 ± 0.1 and scaffold 3D[C_2S/P_6-P_6]C_2S-1Sr was 1.2 ± 0.1 MPa. However, density of the material increases as the material is coated.

In vitro bioactivity

The results of *in vitro* bioactivity for the 3D[C_2S/P_6-P_6]C_2S and 3D[C_2S/P_6-P_6]C_2S-XSr scaffolds, immersed in SBF for differ-

Table 2 – The scaffold's FTIR vibrational modes.

Wavenumber (cm^{-1})	Vibrations
524–611	PO_4^{3-} bending
723–796	$P_2O_7^{4-}$
800	Si—O—Si symmetrical stretching or bending
847	Si—O—2NBO stretching
916	$P_2O_7^{4-}$
936/990	PO_4^{3-} symmetrical stretching
940	Si—O—NBO stretching
1000–1091	PO_4^{3-} asymmetrical stretching
1002–1185	Si—O—Si asymmetrical stretching
1213	$P_2O_7^{4-}$

Refs. [20–23].

ent durations, are depicted in Figs. 8–10. No morphological changes were observed in the 3D[C_2S/P_6-P_6]C_2S microstructure at the beginning of the test, as illustrated in Fig. 8A and B.

After the 14 days in immersion, more pronounced calcium diphosphate polygonal grains were observed due to material degradation as shown in Fig. 8C.

After 21 days of immersion, as shown in Fig. 8D, the polygonal grains disappear, forming a small white precipitate, composed mainly of silicon and the glassy phase was partially dissolved.

After 3 days of immersion, the scaffold 3D[C_2S/P_6-P_6]C_2S-1Sr showed a remarkable difference in morphology with respect to its original structure (Fig. 6B). The observed scaffolds had precipitates with a globular shape covering their entire surface, and the Ca/P ratio of 1.68 was consistent with that of hydroxyapatite-like (HA-like). The amount of P did not vary at 7 and 14 days, meaning that HA-like continued to precipitate over time, however, after 21 days the HA-like fused together forming lamellae on the surface of the scaffold as shown in Fig. 8D. It is important to note that EDX did not detect Sr on the surface, which may be due to the ion being below the detection limit of the equipment.

After 3 days of immersion, the surface of the scaffold 3D[C_2S/P_6-P_6]C_2S-1.5Sr, showed globular morphology but in the form of plates. While, at 7 days it presented in individual form. During 14 days it formed an agglomeration covering the entire HA-like surface. However, after 21 days the agglomeration appeared denser which means that the HA-like precipitated continuously. EDX revealed a Ca/P ratio of 1.60, confirming the presence of HA-like.

After 3 days in SBF, the scaffold 3D[C_2S/P_6-P_6]C_2S-2.5Sr, shows how the scaffold had a drastic change, which did not generate HA-like precipitates on the surface, where part of the coating remained on the calcium diphosphate grains and as the test time passed, no bioactivity was generated. EDX revealed that the Ca/P ratio was 0.97.

Table 3 – Physical properties of the scaffolds.

Sample	Interparticle porosity (%)[a]	Intraparticle porosity (%)[b]	Total microporosity (%)	Macroporosity archimedes principle (%)	Apparent density network (g/cc)	Compressive strength (MPa)
3D[C_2S/P_6-P_6]	20.82	5.03	25.8 ± 0.1	89.1 ± 0.1	2.63	1.2 ± 0.1
3D[C_2S/P_6-P_6]C_2S	24.79	6.86	31.6 ± 0.1	87.4 ± 0.1	2.77	1.0 ± 0.1
3D[C_2S/P_6-P_6]C_2S-1Sr	23.87	8.28	32.1 ± 0.1	86.3 ± 0.1	2.71	1.2 ± 0.1

[a] Corresponding to pores between 1 μm and 300 μm.
[b] Corresponding to pores < 1 μm.

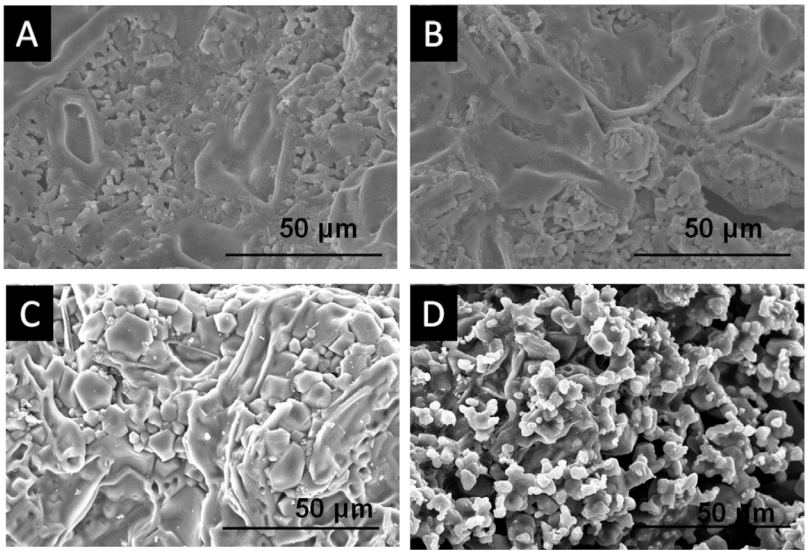

Fig. 8 – SEM micrographs after the *in vitro* bioactivity evaluation of the 3D[C_2S/P_6-P_6]C_2S scaffold (A) 3 days, (B) 7 days, (C) 14 days and (D) 21 days of SBF soaking.

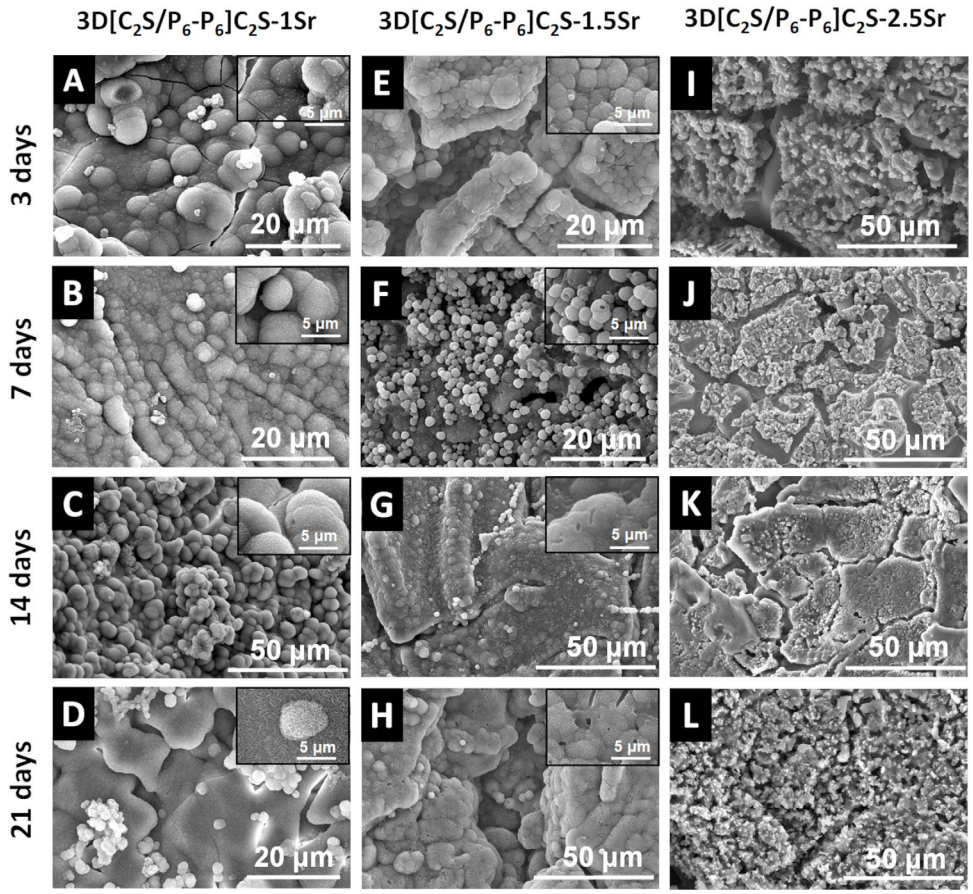

Fig. 9 – SEM micrographs of the 3D[C_2S/P_6-P_6]C_2S-XSr coated scaffolds after different soaking times in SBF. (A–D) 3D[C_2S/P_6-P_6]C_2S-1Sr scaffolds at 3-21days. (E–H) 3D[C_2S/P_6-P_6]C_2S-1.5Sr scaffolds at 3–21days. (I–L) 3D[C_2S/P_6-P_6]C_2S-2.5Sr scaffolds at 3-21days.

Fig. 10 shows the ionic changes after SBF immersion of different doping amounts. The behavior showed that the ion exchange of calcium, phosphorus and silicon was different among the four scaffolds.

In the 3D[C_2S/P_6-P_6]C_2S scaffold, calcium was observed to be released from the scaffold at SBF, phosphorus remained constant in an oscillatory manner during the 21 days of experimentation. However, the concentration of silicon ions had a slight change.

On the contrary, the changes in 3D[C_2S/P_6-P_6]C_2S-1Sr and 3D[C_2S/P_6-P_6]C_2S-1.5Sr scaffolds, were more visible in calcium absorption, however silicon like phosphorus showed opposite behavior, when silicon concentration increased phosphorus concentration decreased.

The 3D[C_2S/P_6-P_6]C_2S-2.5Sr scaffold shows that there are no ionic changes, since the scaffold had a higher percentage of doping that inhibits the exchange.

Discussion

The control of macroporosity and microporosity is an important aspect in obtaining a 3D scaffolds. The presence of a macroporous structure, not only enhances nutrient transport but also creates additional space for cell and tissue growth [25].

The study aimed at creating 3D scaffolds with open porosity interconnected (86–89%) with mechanical properties (0.8–1.6 MPa) similar to trabecular human bone was obtained using the sol–gel in combination with the polymer replication methods [26,27]. Polymeric sponge replication techniques yielded interconnected porous structures with sizes between 2 and 0.75 mm and a strut thickness between 0.35 and 0.45 mm (Fig. 4).

According to the microporosity results, pore sizes ranging from 0.1 µm to 300 µm were obtained (Fig. 7 and Table 3). The pore size is important since other researches mention that the minimum pore size should be more than 100 µm for the support of tissue regeneration. Likewise, the pore size of 300 µm is necessary for the formation of blood vessels during bone regeneration [28].

These scaffolds with the interconnected open porosity, described above, have been obtained using a multilayer scaffold design, based on the following layers: $C_2S/Ca_2P_6O_{17}/C_2S$ (doped and undoped Sr). Where the inner layers $C_2S/Ca_2P_6O_{17}$ denoted core, is designed to provide mechanical properties, while the outer layer of C_2S (doped and undoped Sr) modulates the bioactivity of the scaffold.

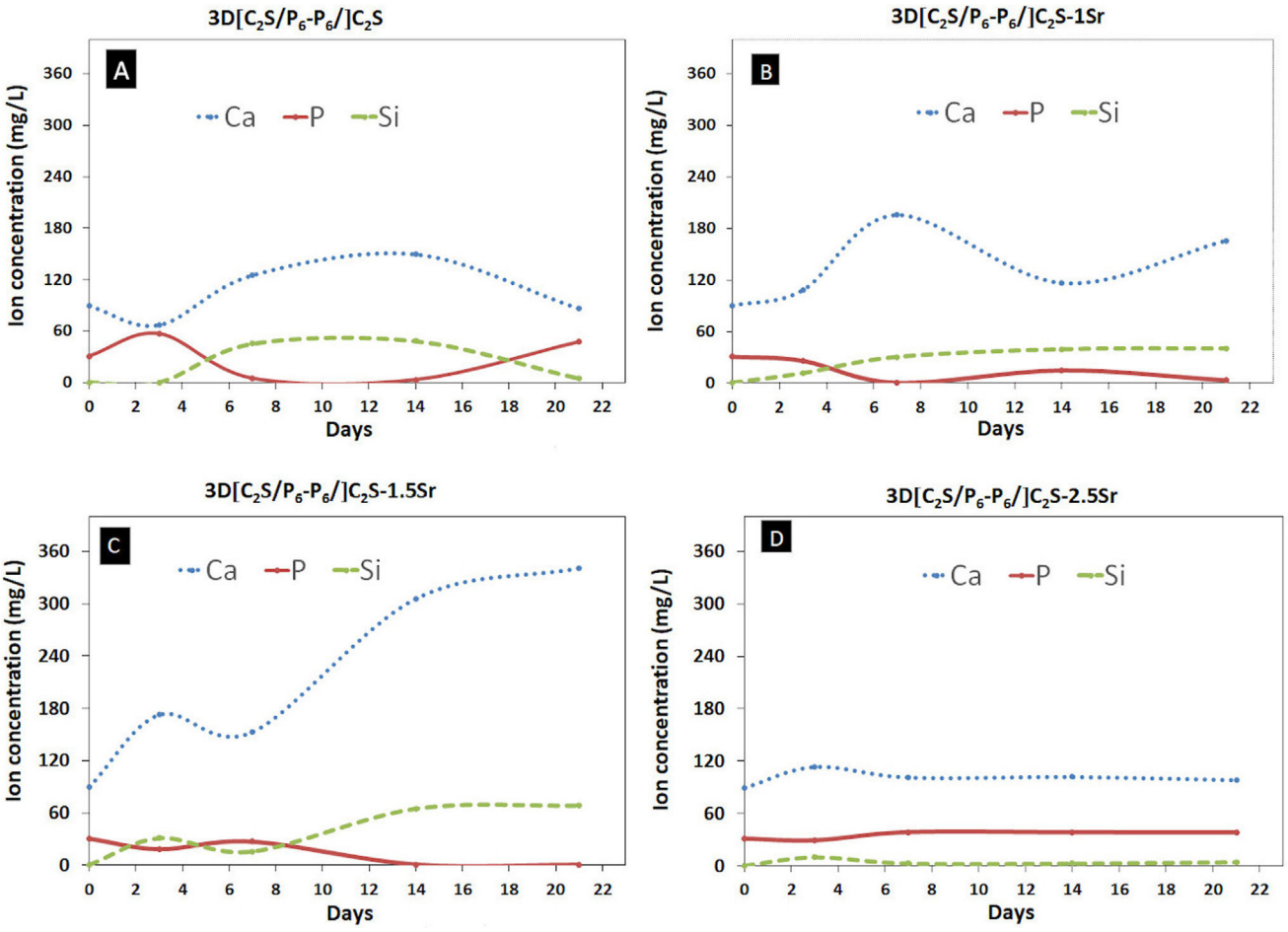

Fig. 10 – Ion concentration changes in SBF during the soakings of the 3D[C_2S/P_6-P_6]C_2S and 3D[C_2S/P_6-P_6]C_2S-XSr coated Scaffolds.

The X-ray diffraction patterns of the inner layer (C_2S) consist mainly of dicalcium silicate (Ca_2SiO_4), and also calcium silicate ($CaSiO_3$). A glass ($Ca_2P_6O_{17}$) was then applied as a coating, resulting in 3D[C_2S/P_6-P_6]. The new scaffolds (3D[C_2S/P_6-P_6] core) showed a shiny appearance (Fig. 4C) due to the high glass content, obtaining a 0.8–1.6 MPa compression resistance. This second coating affects the inner C_2S layer, obtaining new calcium diphosphate, cristobalite and tricalcium phosphate phases (Fig. 1). The cristobalite is generated when C_2S yields calcium ions, transforming part of the glassy phase into calcium pyrophosphate and tricalcium phosphate, thus obtaining a glass-ceramic. One possible explanation for this behavior is that P6 is made up of infinitely polymeric layers of 14-membered rings of P04-tetrahedrons. Each ring contains 6 three-cornered and 8 two-cornered linked tetrahedra. This structure has higher energy than a single phase such as calcium pyrophosphate or tricalcium phosphate [29].

The high glass content of the scaffold when in contact with the SBF generates a very fast hydrolysis which generates an ionic environment not suitable for HA generation. Therefore, a chemical attack was carried out to remove the excess of glassy phase from the scaffold, without significantly affecting the mechanical properties which remain in the range of 0.8–1.5 MPa (Table 3). Then assessing the mineralogical composition of the nucleus before and after chemical attack, we observed slight discrepancies in the diffraction patterns. Specifically, the intensity of the peaks related to the calcium pyrophosphate phase decreased after chemical attack. Fig. 1confirms these findings. The microstructure of the different layers of the scaffolds shown in Figs. 5 and 6 correspond to the main ones obtained by XRD.

In order to modulate the bioactivity, a third layer of C_2S was applied. XRD shows an increase in the tricalcium phosphate phase (Fig. 2). This behavior is due to the fact that the C_2S in the last layer acts as an additional source of calcium, transforming part of the existing glassy phase into tricalcium phosphate and calcium pyrophosphate. The presence of calcium pyrophosphate in the scaffold [C_2S/P_6-P_6]C_2S (Fig. 2) inhibits bioactivity (Fig. 7). Studies have shown that pyrophosphate has an inhibitory effect on crystallization in a laboratory setting, but not within a living organism. This difference is mainly due to the presence of the tissue-specific enzyme alkaline phosphatase (TNAP) *in vivo*. TNAP catalyses the breakdown of pyrophosphate into two phosphate molecules, which facilitates bone mineralization [30].

In order to modulate the bioactivity, strontium (Sr = 0–0.25 wt) is added to the outer layer of the C_2S. The addition of Sr causes a decrease in calcium pyrophosphate as non-stoichiometric Sr phosphate phases appear.

As can be seen in Fig. 8, the scaffolds with [C_2S/P_6-P_6]C_2S-1Sr and [C_2S/P_6-P_6] C_2S-1.5Sr show bioactivity at 3 days presenting a globular morphology precipitate of HA-like. However, when the Sr content is increased to the concentration of the scaffold [C_2S/P_6-P_6] C_2S-2.5Sr, the bioactivity is lost, possibly due to the amount of Sr incorporated in the HA-like precipitate structure. Although Sr is not detected in EDX (due to its small concentration), it seems that the difference in ionic radius between the Sr ion (larger ionic radius) and the Ca ion, is sufficiently high for this incorporation to generate tensions in the HA-like structure, preventing its precipitate. This effect of Sr has been described in the literature in other materials [14,15]. It has also been observed with other smaller ions such as magnesium where the bioactivity is modulated depending on the concentration [3,16,17]. This effect is so important that it modifies the morphology of the precipitate, obtaining HA structures consisting in some cases of hollow spheres [4].

However, biocompatibility tests have to be performed to study the behavior of the cells and even of a living bone tissue by implantation in animals. This study highlights the possible application of this new 3D multilayer scaffolds with open porosity interconnected C_2S/$Ca_2P_6O_{17}$/C_2S doped with several amounts of Sr (Sr = 0–2.5 wt%) for bone tissue engineering.

Conclusions

The new 3D multilayer ceramic scaffolds were fabricated by sol–gel and polymer replication methods. A 3D[C_2S/P_6-P_6] core was developed as a base which were coated with multiple layers of [C_2S/P_6-P_6]C_2S-XSr (X = 1, 1.5, and 2.5 wt%).

The scaffold's multilayer core offered three-dimensional mechanical strength and porosity, which were crucial for sustaining the external coatings that enhanced its bioactivity.

It was possible to modulate the bioactivity of the scaffolds from an initially non-bioactive material such as the 3D[C_2S/P_6-P_6]C_2S to scaffolds with variable bioactivity depending on the strontium content.

Of all the coated scaffolds prepared, 3D[C_2S/P_6-P_6]C_2S-1Sr was considered to be the most bioactive, as HA-like was formed before 24 h due to the incorporation of Sr^{2+} in the scaffolds. This resulted in the precipitated HA-like being similar to the biological hydroxyapatite present in human bone, potentially allowing for better cell adhesion.

Acknowledgements

This work is part of the project PID2020-116693RB-C21, funded by MCIN/AEI/10.13039/501100011033 Spain. Also grant CIAICO/2021/157 funded by the Generalitat Valenciana Spain.

REFERENCES

[1] H. Qu, H. Fu, Z. Han, Y. Sun, Biomaterials for bone tissue engineering scaffolds: a review, RSC Adv. 9 (45) (2019) 26252–26262, http://dx.doi.org/10.1039/c9ra05214c.
[2] J.J. Li, D.L. Kaplan, H. Zreiqat, Scaffold-based regeneration of skeletal tissues to meet clinical challenges, J. Mater. Chem. B 2 (42) (2014) 7272–7306, http://dx.doi.org/10.1039/c4tb01073f.
[3] N.A. Mata, M. Arango-Ospina, P. Velasquez, A. Murciano, P.N.A. De Aza, R. Boccaccini, Effect of Sr, Mg and Fe substitution on the physico-chemical and biological properties of Si Ca P multilayer scaffolds, Bol. Soc. Esp. Ceram. Vidrio 62 (2) (2023) 145–159, http://dx.doi.org/10.1016/j.bsecv.2021.11.005.
[4] E. Sebastian, A. Murciano, P.N. De Aza, P.P. Velasquez, Synthesis of 3D porous ceramic scaffolds obtained by the sol–gel method with surface morphology modified by hollow spheres for bone tissue engineering applications, Ceram. Inter. 49 (2023) 4393–4402, http://dx.doi.org/10.1016/j.ceramint.2022.09.326.
[5] V.M. Schatkoski, et al., Current advances concerning the most cited metal ions doped bioceramics and silicate-based bioactive glasses for bone tissue engineering, Ceram. Int. 47 (3) (2021) 2999–3012, http://dx.doi.org/10.1016/j.ceramint.2020.09.213.
[6] A. Wubneh, E.K. Tsekoura, C. Ayranci, H. Uludağ, Current state of fabrication technologies and materials for bone tissue engineering, Acta Biomater. 80 (2018) 1–30, http://dx.doi.org/10.1016/j.actbio.2018.09.031.
[7] P. Valerio, M.M. Pereira, A.M. Goes, M.F. Leite, The effect of ionic products from bioactive glass dissolution on osteoblast proliferation and collagen production, Biomaterials 25 (15) (2004) 2941–2948, http://dx.doi.org/10.1016/j.biomaterials.2003.09.086.
[8] K. Ariane, A. Tamayo, A. Chorfa, F. Rubio, J. Rubio, Efecto de P_2O_5 y Al_2O_3 sobre la cristalización, estructura, microestructura y propiedades de las vitrocerámicas Li_2O–MgO–Al_2O_3–SiO_2–TiO_2–ZrO_2, Bol. Soc. Esp. Ceram. Vidrio. 61 (2) (2022) 146–159, http://dx.doi.org/10.1016/j.bsecv.2020.08.004.
[9] D. Ke, S. Tarafder, S. Vahabzadeh, S. Bose, Effects of MgO, ZnO SrO, and SiO_2 in tricalcium phosphate scaffolds on in vitro gene expression and in vivo osteogenesis, Mater. Sci. Eng. C 96 (2019) 10–19, http://dx.doi.org/10.1016/j.msec.2018.10.073.
[10] G. Kaur, et al., Mechanical properties of bioactive glasses, ceramics, glass-ceramics and composites: state-of-the-art review and future challenges, Mater. Sci. Eng. C 104 (2019) 109895, http://dx.doi.org/10.1016/j.msec.2019.109895.
[11] M.S.N. Shahrbabak, F. Sharifianjazi, D. Rahban, A. Salimi, A comparative investigation on bioactivity and antibacterial properties of sol–gel derived 58S bioactive glass substituted by Ag and Zn, Silicon 11 (2019) 2741–2751, http://dx.doi.org/10.1007/s12633-018-0063-2.
[12] S.M. Rabiee, N. Nazparvar, M. Azizian, D. Vashaee, L. Tayebi, Effect of ion substitution on properties of bioactive glasses: a review, Ceram. Int. 41 (6) (2015) 7241–7251, http://dx.doi.org/10.1016/j.ceramint.2015.02.140.
[13] N.A. Mata, P. Ros-Tárraga, P. Velasquez, A. Murciano, P.N. De Aza, Synthesis and characterization of 3D multilayer porous Si–Ca–P scaffolds doped with Sr ions to modulate *in vitro* bioactivity, Ceram. Inter. 46 (1) (2020) 968–977, http://dx.doi.org/10.1016/j.ceramint.2019.09.058.
[14] A. Moghanian, R. Portillo-Lara, E. Shirzaei, Synthesis and characterization of osteoinductive visible light-activated

adhesive composites with antimicrobial properties, J. Tissue Eng. Regen. Med. 14 (2020) 66–81, http://dx.doi.org/10.1002/term.2964.
[15] M.S. Araujo, A.C. Silva, B. Cabal, J.F. Bartolomé, S. Mello-Castanho, In vitro bioactivity and antibacterial capacity of 45S5 Bioglass®-based compositions containing alumina and strontium, J. Mater. Res. Technol., 13, 154–161, doi:10.1016/j.jmrt.2021.04.053.
[16] A. Moghanian, M. Zohourfazeli, M.H. Mahdi Tajer, Z. Miri, S. Hosseini, A. Rashvand, Preparation, characterization and in vitro biological response of simultaneous co-substitution of Zr^{+4}/Sr^{+2} 58S bioactive glass powder, Ceram. Inter. 47 (17) (2021) 23762–23769, http://dx.doi.org/10.1016/j.ceramint.2020.11.139.
[17] D.W. Kim, J.S. An, I.S. Cho, Effects of Mg and Sr co-addition on the densification and biocompatible properties of calcium pyrophosphate, Ceram. Int. 44 (8) (2018) 9689–9695, http://dx.doi.org/10.1016/j.ceramint.2018.02.198.
[18] I. Ullah, et al., Simultaneous co-substitution of Sr^{2+}/Fe^{3+} in hydroxyapatite nanoparticles for potential biomedical applications, Ceram. Int. 44 (17) (2018) 21338–21348, http://dx.doi.org/10.1016/j.ceramint.2018.08.187.
[19] ISO/FDIS 23317 standard. Implants for Surgery-In Vitro Evaluation for Apatite-Forming Ability of Implant. https://www.iso.org/standard/36406.html.
[20] P.N. De Aza, F. Guitian, C. Santos, S. De Aza, R. Cusco, L. Artus, Vibrational properties of calcium phosphate compounds II. comparation between hydroxyapatite and β-tricalcium phosphate, Chem. Mater. 9 (1997) 916–922, http://dx.doi.org/10.1021/cm9604266.
[21] F. Ren, Y. Ding, Y. Leng, Infrared spectroscopic characterization of carbonated apatite: a combined experimental and computational study, J. Biomed. Mater. Res. A 102 (2014) 496–505, http://dx.doi.org/10.1002/jbm.a.34720.
[22] H. Aguia, J. Serra, P. Gonzalez, B. Leon, Structural study of sol–gel silicate glasses by IR and Raman spectroscopies, J. Non-Cryst. Solids 355 (8) (2009) 475–480, http://dx.doi.org/10.1016/j.jnoncrysol.2009.01.010.
[23] P. Innocenzi, Infrared spectroscopy of sol–gel derived silica-based films: a spectramicrostructure overview, J. Non-Cryst. Solids 316 (2003) 309–319, http://dx.doi.org/10.1016/S0022-3093(02)01637-X.
[24] S. Raynaud, E. Champion, D. Bernache-Assollant, P. Thomas, Calcium phosphate apatites with variable Ca/P atomic ratio I Synthesis, characterisation and thermal stability of powders, Biomaterials 23 (4) (2002) 1065–1072, http://dx.doi.org/10.1016/S0142-9612(01)00218-6.
[25] Q. Nawaz, A. de Pablos-Martín, A.T. Contreras Jaimes, F. Scheffler, T. Wagner, D.S. Brauer, A.R. Boccaccini, Comparison of microstructure, sintering behavior, and biological response of sol–gel and melt-derived 13-93 bioactive glass scaffolds, Open Ceram. 15 (100407) (2023), http://dx.doi.org/10.1016/j.oceram.2023.100407.
[26] G. Kaur, et al., Mechanical properties of bioactive glasses, ceramics, glass-ceramics and composites: state-of-the-art review and future challenges, Mater. Sci. Eng. C104 (2019) 109895, http://dx.doi.org/10.1016/j.msec.2019.109895.
[27] P. Ros-Tarraga, N.A. Mata, A. Murciano, P. Velasquez, P.N. De Aza, Multilayer materials: a method to link bioactivity and durability, Ceram. Int. 45 (17) (2019) 23611–23618, http://dx.doi.org/10.1016/j.ceramint.2019.08.072.
[28] N. Abbasi, S. Hamlet, R.M. Love, N.T. Nguyen, Porous scaffolds for bone regeneration review, J. Sci. Adv. Mater. Dev. 5 (1) (2020) 1–9, http://dx.doi.org/10.1016/j.jsamd.2020.01.007.
[29] D. Stachel, H. Paulus, I. Svoboda, H. Fuess, Crystal structure of calcium ultraphosphate $Ca_2P_6O_{17}$, Zeitschr. Kristallogr. 202 (1992) 117–118.
[30] C. Slater, D. Laurencin, V. Burnell, M.E. Smith, L.M. Grover, J.A. Hriljac, A.J. Wright, Enhanced stability and local structure in biologically relevant amorphous materials containing pyrophosphate, J. Mater. Chem. 21 (46) (2011) 18783, http://dx.doi.org/10.1039/c1jm13930d.